Medium characterization from interface-wave impedance and ellipticity using simultaneous displacement and pressure measurements

K. N. van Dalen,[a] G. G. Drijkoningen, D. M. J. Smeulders, and H. K. J. Heller
Faculty of Civil Engineering and Geosciences, Department of Geotechnology, Delft University of Technology, Stevinweg 1, 2628 CN Delft, The Netherlands

C. Glorieux, B. Sarens, and B. Verstraeten
Department of Physics and Astronomy, Laboratory of Acoustics and Thermal Physics, Katholieke Universiteit Leuven, Celestijnenlaan 200D, 3001 Heverlee, Belgium

(Received 3 November 2010; revised 10 May 2011; accepted 24 May 2011)

The interface-wave impedance and ellipticity are wave attributes that interrelate the full waveforms as observed in different components. For each of the fluid/elastic-solid interface waves, i.e., the pseudo-Rayleigh (*pR*) and Stoneley (*St*) waves, the impedance and ellipticity are found to have different functional dependencies on Young's modulus and Poisson's ratio. By combining the attributes in a cost function, unique and stable estimates of these parameters can be obtained, particularly when using the *St* wave. In a validation experiment, the impedance of the laser-excited *pR* wave is successfully extracted from simultaneous measurements of the normal particle displacement and the fluid pressure at a water/aluminum interface. The displacement is measured using a laser Doppler vibrometer (LDV) and the pressure with a needle hydrophone. Any LDV measurement is perturbed by refractive-index changes along the LDV beam once acoustic waves interfere with the beam. Using a model that accounts for these perturbations, an impedance decrease of 28% with respect to the plane wave impedance of the *pR* wave is predicted for the water/aluminum configuration. Although this deviation is different for the experimentally extracted impedance, there is excellent agreement between the observed and predicted *pR* waveforms in both the particle displacement and fluid pressure. © *2011 Acoustical Society of America*. [DOI: 10.1121/1.3605537]

PACS number(s): 43.35.Pt, 43.35.Ud, 43.58.Bh, 43.40.Sk [ANN] Pages: 1299–1312

I. INTRODUCTION

Interface waves that travel along the boundary of a medium carry information of the acoustic parameters. The waves can be utilized to determine these parameters *in situ*. Applications exist in many different fields and scales, e.g., in non-destructive testing of materials and structures, borehole logging in geotechnical and reservoir engineering, surface seismics in geophysics, and seismology.

For medium characterization, often simply the propagation velocity and the attenuation of an interface wave are employed.[1,2] In that case, a single-component measurement is sufficient, e.g., the detection of the normal particle velocity induced by the waves. The full waveforms of an interface wave as present in different components exhibit, however, particular properties that are also worth exploiting in medium characterization. Typically, the well-known Rayleigh wave at the vacuum/elastic-solid interface induces a retrograde elliptical motion of the material particles at the interface.[3] The ratio of the principal axes of the corresponding ellipse is a function of Poisson's ratio only.[4] In order to extract the ellipticity, which is defined as the spectral ratio of the tangential and normal particle displacements at the interface,[4–6] one needs to record at least two components of the particle displacement. For the "pseudo-" Rayleigh (*pR*) wave and the Stoneley (*St*) wave that exist at the fluid/elastic-solid interface,[2,3,7–9] in addition to the ellipticity the impedance can be distinguished, defined as the spectral ratio of the fluid pressure and the normal component of the particle velocity at the interface.[10] Obviously, for the extraction of the interface-wave impedance also a two-component measurement is required.

Nishizawa *et al.*[11] have measured two components of an ultrasonic wave field at an interface using laser Doppler vibrometers. Two mutually orthogonal beams at 45° incidence, and a normally incident beam were applied to detect the tangential and normal components, respectively. In general, ultrasonic laser interferometers and vibrometers give reliable absolute values of particle displacement or velocity, and have particular advantages, i.e., physical coupling to the sample is not required, they have a broadband response and a sub-millimeter focal-point size.[12] Recently, the elliptical particle motion of the Rayleigh wave has successfully been measured using an adaptive laser interferometer by Blum *et al.*,[13] by applying only one laser beam and taking advantage of the surface roughness of the sample that causes the light to scatter away from the incidence direction. Further, in several publications it is shown that laser ultrasonics can be used to detect the *pR* and *St* waves at fluid/elastic-solid interfaces.[2,14,15]

Laser ultrasonics can also be applied to assess the acoustic pressure at the fluid/elastic-solid interface by using a

[a]Author to whom correspondence should be addressed. Electronic mail: k.n.vandalen@tudelft.nl

Doppler beam skimming over the surface, normal to the direction of propagation of the wave field.[16,17] Then, using the photoelastic effect, the recorded signal can be converted into acoustic pressure.[18] However, the involved length of the acoustic wavefront is quite difficult to estimate, which makes the absolute values of the pressure rather uncertain.

The goal of this paper is to show the feasibility of characterizing an elastic solid by simultaneously using the impedance and ellipticity of each of the ultrasonic *pR* and *St* waves at the fluid/elastic-solid interface.

To this end, we first define the impedance and ellipticity of the *pR* and *St* waves theoretically and show that they have different functional dependencies on Young's modulus and Poisson's ratio, for each of the wavemodes. By combining the impedance and ellipticity in a cost function, we take advantage of this difference and show that unique estimates of Young's modulus and Poisson's ratio can be obtained simultaneously.

Motivated by this result, we show the feasibility of the extraction of interface-wave impedance from simultaneous normal particle displacement and fluid pressure measurements at ultrasonic frequencies. We restrict ourselves to the extraction of impedance because the extraction of ellipticity has already been performed successfully. We present an experimental setup using a laser Doppler vibrometer (LDV) for the particle displacement measurement and a needle hydrophone to record the absolute values of the fluid pressure. For a water/aluminum configuration, we show how the impedance of the *pR* wave can be successfully extracted from the measurements.

Finally, we compare the experimentally observed waveforms with the modeled predictions obtained using the Cagniard–de Hoop method.[7] In the model we account for the interference of the acoustic waves in the fluid and the LDV beam that crosses the fluid. The laser light is perturbed by the pressure-induced refractive-index changes. The integrated effect of all perturbations along the beam is an additional contribution to the displacement measurement, which can be quite substantial.[19] We quantify the influence on the predicted waveforms and on the extracted *pR* wave impedance, and discuss the effect of the involved measurement inaccuracies in the impedances and ellipticities on the estimated values of Young's modulus and Poisson's ratio.

In Sec. II we define the impedance and ellipticity, and illustrate their behaviors. We show how Young's modulus and Poisson's ratio can be estimated in Sec. III. Then, in Sec. IV we give expressions for the acoustic response and derive an expression for the additional contribution to the LDV measurement. We show the experimental results and the extracted impedance in Sec. V and compare them with modeled predictions in Sec. VI. The effect of inaccuracies is discussed in Secs. III and VII, and conclusions are given in Sec. VIII.

II. IMPEDANCE AND ELLIPTICITY

In this section we define expressions for the impedances and ellipticities associated with the *pR* and *St* waves at the fluid/elastic-solid interface. We use the plane-wave domain solutions of the governing equations that correspond to interface waves and illustrate the dependencies of the impedance and ellipticity on Young's modulus and Poisson's ratio for each of the wavemodes.

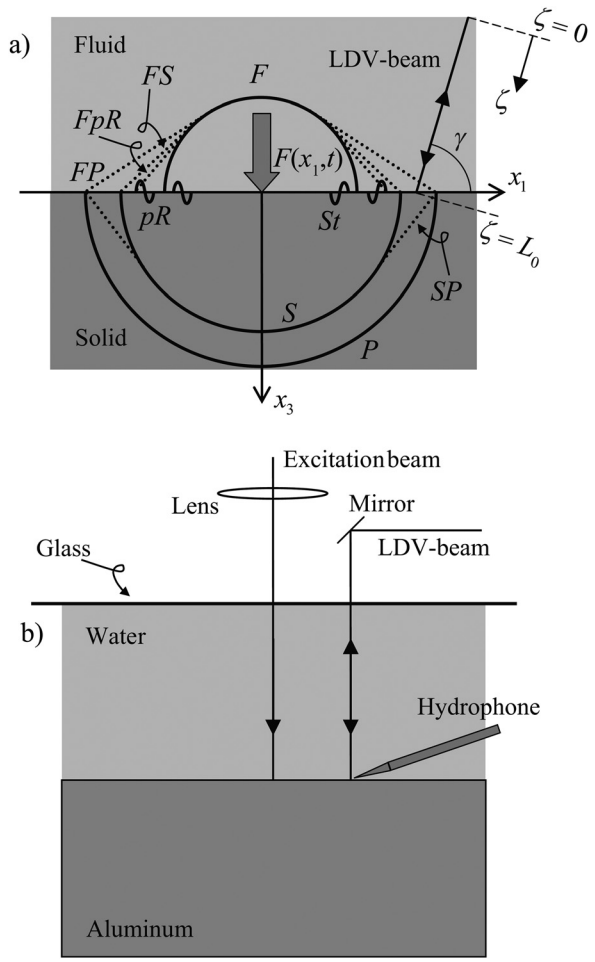

FIG. 1. (a) Fluid/elastic-solid configuration, model for the acoustic response excited by a laser [modeled as normal force $F(x_1,t)$] and schematic response: compressional (*P*) wave, shear (*S*) wave, fluid (*F*) wave, pseudo-Rayleigh (*pR*) wave, and Stoneley (*St*) wave. Double-mode symbols (e.g., *SP*) indicate lateral waves (dotted lines): the first symbol denotes the wavemode of the specific arrival; the second denotes the one from which it is radiated. The position of the laser Doppler vibrometer (LDV) beam with general orientation (angle γ) is determined by the local ζ axis. (b) Schematic overview of the experimental setup used for the simultaneous detection of waves at the water/aluminum interface.

Let us define the physical model and the corresponding solution. We consider a fluid half-space on top of an elastic solid [see Fig. 1(a); the response and the LDV beam are discussed later]. Both media are homogeneous and isotropic. The behavior of the elastic solid ($x_3 > 0$) is governed by the following elastic wave equation[20]

$$\rho\partial_t^2\mathbf{u} = (\lambda + 2\mu)\nabla\nabla\cdot\mathbf{u} - \mu\nabla\times\nabla\times\mathbf{u}, \tag{1}$$

where $\partial_t = \partial/\partial t$, λ and μ are the Lamé constants, ρ denotes the material density, and $\mathbf{u}(\mathbf{x},t) = (u_1,u_3)^T$ is the particle displacement vector (the superscript T denotes transposition). We assume a two-dimensional wave motion because this is sufficient to define the impedances and ellipticities of the interface waves, and because the experimentally observed wave motion approximates two-dimensional wave propagation (see Sec.

IV). The behavior of the fluid ($x_3 < 0$) is governed by the acoustic wave equation[21]

$$\rho_F \partial_t^2 p_F = K_F \nabla^2 p_F, \tag{2}$$

where K_F and ρ_F denote the bulk modulus and density of the fluid, respectively, and p_F denotes the fluid pressure.

The boundary conditions at the fluid/elastic-solid interface comprise the continuity of the normal component of particle displacement, continuity of the normal component of the traction, and the vanishing of the tangential component of the traction in the solid. Incorporating a force acting normally on the boundary $F(x_1,t)$ (Nm^2) to excite waves [Fig. 1(a)], in the limit of $x_3 \to 0$ the following conditions should be satisfied:

$$u_3 - U_{F,3} = 0, \tag{3}$$

$$\tau_{33} + p_F = -F(x_1, t), \tag{4}$$

$$\tau_{13} = 0. \tag{5}$$

Here, $U_{F,3}$ is the vertical component of the fluid particle displacement $\mathbf{U}_F(\mathbf{x},t)$ and τ_{ij} is the stress tensor in the solid.

We apply the Fourier transform over time t and horizontal coordinate x_1 according to

$$\tilde{\tilde{\mathbf{u}}}(k_1, x_3, \omega) = \int_{-\infty}^{\infty}\int_{-\infty}^{\infty} \mathbf{u}(\mathbf{x}, t)\exp(-\mathrm{i}(\omega t - k_1 x_1))dtdx_1, \tag{6}$$

where ω denotes the angular frequency, k_1 is the horizontal angular wavenumber and i is the imaginary unit. Because $\mathbf{u}(\mathbf{x},t)$ is real-valued it is sufficient to consider $\omega \geq 0$ only. The transforms are also applied to the other field quantities. In this section we use $k_1 = \omega p_1$, where p_1 is the horizontal slowness, because this enables us to show that the characteristic determinant (see further), and the impedance and ellipticity derived from that, are independent of frequency. The combined bar/tilde refers to the (k_1, x_3, ω) domain, and a single tilde refers to the (p_1, x_3, ω) domain.

In the (p_1,x_3,ω) domain, the wave fields in the lower and upper media are described by physically relevant solutions of the acoustic and elastic wave equations [Eqs. (1) and (2)], respectively, according to[7,20]

$$\tilde{u}_1 = \frac{p_1}{\mathrm{i}\omega}\tilde{A}_P\tilde{F}\exp(-\mathrm{i}\omega q_P x_3) + \frac{q_S}{\mathrm{i}\omega}\tilde{A}_S\tilde{F}\exp(-\mathrm{i}\omega q_S x_3), \tag{7}$$

$$\tilde{u}_3 = \frac{q_P}{\mathrm{i}\omega}\tilde{A}_P\tilde{F}\exp(-\mathrm{i}\omega q_P x_3) - \frac{p_1}{\mathrm{i}\omega}\tilde{A}_S\tilde{F}\exp(-\mathrm{i}\omega q_S x_3), \tag{8}$$

for $x_3 > 0$, and

$$\tilde{p}_F = \tilde{A}_F\tilde{F}\exp(+\mathrm{i}\omega q_F x_3), \tag{9}$$

for $x_3 < 0$. Here $q_\alpha = \left(s_\alpha^2 - p_1^2\right)^{1/2}$, with $\alpha = \{P, F, S\}$, are the vertical slownesses having $\mathrm{Im}(q_\alpha) \leq 0$ for real p_1, and s_α are the corresponding body-wave slownesses being the reciprocals of the phase velocities ($c_\alpha = 1/s_\alpha$). The complex-valued amplitude factors $\tilde{A}_\alpha$ are determined by the boundary conditions. Using the momentum equation of the fluid and the stress–strain relation of the elastic solid,[20,21] the following set of equations for the $\tilde{A}_\alpha$ is obtained:

$$\begin{bmatrix} q_P & q_F/\rho_F & -p_1 \\ \mu\left(s_S^2 - 2p_1^2\right) & -1 & -2\mu p_1 q_S \\ 2p_1 q_P & 0 & s_S^2 - 2p_1^2 \end{bmatrix}\begin{bmatrix} \tilde{A}_P \\ \tilde{A}_F \\ \tilde{A}_S \end{bmatrix} = \begin{bmatrix} 0 \\ 1 \\ 0 \end{bmatrix}. \tag{10}$$

The solution can be easily found and reads

$$\tilde{A}_P = +\frac{s_S^2}{\rho}\frac{s_S^2 - 2p_1^2}{\Delta_{St}}, \tag{11}$$

$$\tilde{A}_F = -\frac{\rho_F}{\rho}\frac{q_P}{q_F}\frac{s_S^4}{\Delta_{St}}, \tag{12}$$

$$\tilde{A}_S = -\frac{s_S^2}{\rho}\frac{2p_1 q_P}{\Delta_{St}}, \tag{13}$$

where Δ_{St} is the characteristic determinant of the matrix in Eq. (10),

$$\Delta_{St} = \Delta_R + s_S^4\frac{q_P}{q_F}\frac{\rho_F}{\rho}, \tag{14}$$

which is the "Stoneley-wave denominator" of the fluid/elastic-solid interface[7] (or "Scholte-wave denominator"). It contains the "Rayleigh-wave denominator,"

$$\Delta_R = \left(s_S^2 - 2p_1^2\right)^2 + 4p_1^2 q_S q_P, \tag{15}$$

which is associated with the stress-free vacuum/solid interface.[20]

The signs of the roots q_P, q_F, and q_S are very important to obtain the proper solutions (zeros) for the interface wave slownesses in Eq. (14). The *St* wave is a "true" interface wave that propagates only along the interface and decays with distance from the interface. The zero of the Stoneley denominator [Eq. (14)] related to the *St* wave ($p_1 = s_{St}$), which forms the *St* pole in the response [Eqs. (7)–(9)], is found on the real p_1 axis at $s_{St} > s_F$ and lies on the Riemann sheet where $\mathrm{Im}(q_\alpha) \leq 0$ (principal Riemann sheet).[7] The pseudo-Rayleigh (*pR*) wave is a "pseudo" interface wave that radiates a fluid wavefront as it propagates along the interface [see Fig. 1(a): *FpR* front], and decays with distance from the interface into the solid. The zero of Eq. (14) related to the *pR* wave ($p_1 = s_{pR}$) is complex-valued with $\mathrm{Im}(s_{pR}) < 0$ and lies on the Riemann sheet where $\mathrm{Im}(q_F) > 0$ and $\mathrm{Im}\left(q_{P,S}\right) \leq 0$.[3,22,23] The phase velocity and attenuation of the interface waves are fully characterized by these slownesses, i.e., by their real and imaginary parts, and, at the interface, their far-field waveforms are fully captured by the residue contributions of the corresponding poles once the response [Eqs. (7)–(9)] is transformed to the $(\mathbf{x},t)$ domain.[23]

Consequently, we can define the impedance and ellipticity in (p_1,x_3,ω) domain by the spectral ratio of two components for $x_3 = 0$, evaluated at the specific slownesses s_β,

where $\beta = \{pR, St\}$. Evaluation of the full waveforms, which often implies the evaluation of integrals numerically, is not required. Still, the particular information present in the multi-component waveforms of an interface wave is captured by these wave attributes and can be easily exploited (see Sec. III). We define the impedance I_β as the spectral ratio of the fluid pressure and the normal particle velocity at the interface, which expresses the resistance to the particle motion induced by the particular wave,[24] and the ellipticity E_β as the spectral ratio of the tangential and the normal particle displacements (so-called H/V ratio).[4] The result can be written as

$$I_\beta = \left.\frac{\tilde{p}_F}{\mathrm{i}\omega\tilde{u}_3}\right|_{p_1=s_\beta,x_3=0} = -\left.\frac{\rho_F}{q_F}\right|_{p_1=s_\beta}, \tag{16}$$

$$E_\beta = \left.\frac{\tilde{u}_1}{\tilde{u}_3}\right|_{p_1=s_\beta,x_3=0} = \left.\frac{p_1}{q_P}\frac{s_S^2 - 2p_1^2 - 2q_P q_S}{s_S^2}\right|_{p_1=s_\beta}. \tag{17}$$

We note that both the impedances and ellipticities are independent of frequency as the model is non-dispersive in nature.

We have now defined the impedances and ellipticities in the (p_1, x_3, ω) domain [Eqs. (16) and (17)]. Their expressions are independent of the properties of the force as it is divided out. Therefore, the quantities are solely attributes of the waves. In the $(\mathbf{x},\omega)$ domain the expressions also correctly describe the ratios of the components as the source is divided out as well. The quantities can be referred to as the plane-wave or far-field impedances and ellipticities, respectively.[10]

In the limiting case of a free surface (vacuum/elastic solid), only the Rayleigh wave can exist, which is a true interface wave. The corresponding zero of Eq. (15) lies on the Riemann sheet where $\mathrm{Im}(q_{P,S}) \leq 0$. The ellipticity E_R follows from Eq. (17) for $\Delta_R(p_1 = s_R) = 0$ and reads[4,25,26]

$$E_R = -\left.\frac{2p_1 q_S}{s_S^2 - 2p_1^2}\right|_{p_1=s_R,x_3=0} = -2\mathrm{i}\frac{\left(1 - s_S^2/s_R^2\right)^{1/2}}{2 - s_S^2/s_R^2}, \tag{18}$$

where s_R is the slowness of the Rayleigh wave with $s_R > s_S$. The Rayleigh-wave ellipticity is a function of Poisson's ratio only.[4] From Eq. (18) it can be observed that $\tilde{u}_1$ and $\tilde{u}_3$ have exactly a $\pi/2$ phase difference, i.e., $\angle(E_R) = -\pi/2$, which indicates retrograde elliptical particle motion associated with the Rayleigh wave. The corresponding ellipse has principal axes that are oriented normally and tangentially to the interface, respectively.[25]

In Fig. 2 we depict the magnitudes of the impedances and ellipticities of the pR and St waves (fluid/elastic solid) as a function of Young's modulus E and Poisson's ratio ν. The values of the non-varying material parameters are taken according to a water/aluminum configuration (see Table I). The magnitudes of I_{pR} and I_{St} are mainly dependent on E (variation mainly in E direction). The magnitudes of E_{pR} and E_{St} are, however, mainly dependent on ν, similar to the ellipticity of the "true" Rayleigh wave. The phases of I_{pR} and E_{pR} vary only slightly over the (E,ν) domain (and are therefore not displayed): $\angle(I_{pR}) \cong \pi$, which implies that the pressure and the normal particle velocity induced by the pR wave are out of phase; $\angle(E_{pR}) \cong -\pi/2$, implying that the particle motion is retrograde elliptical as for the true Rayleigh wave, but the principal axes of the ellipse are slightly rotated as the phase difference between $\tilde{u}_1$ and $\tilde{u}_3$ is not exactly $\pi/2$, due to s_{pR} being complex-valued.[25] The phases of the attributes of the St wave are constant, i.e., $\angle(I_{St}) = -\pi/2$ and $\angle(E_{St}) = -\pi/2$. The latter equality shows that the St wave also induces a retrograde elliptical particle motion.

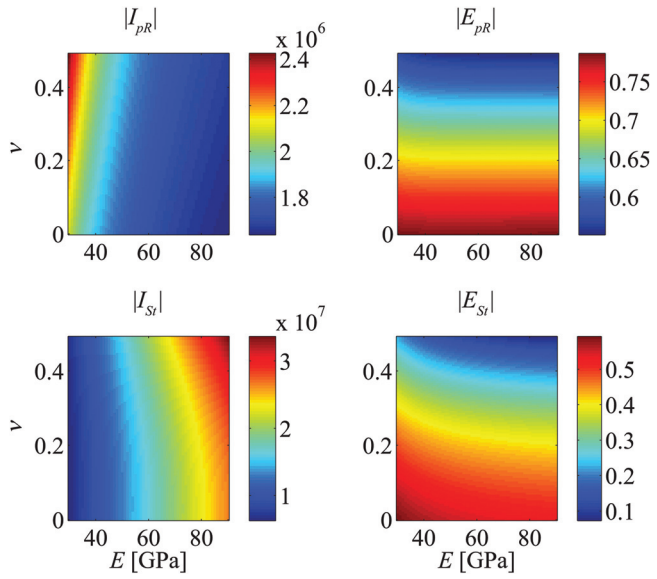

FIG. 2. Impedances I_β and ellipticities E_β of the pseudo-Rayleigh and Stoneley waves $[\beta = \{pR, St\}]$ at the fluid/elastic-solid interface as a function of Young's modulus E and Poisson's ratio ν. Only the magnitudes are shown.

In this section, we have only shown the behaviors of the impedances and ellipticities in the (E,ν) domain. The

TABLE I. Values of material parameters of aluminum (Young's modulus E, Poisson's ratio ν, density ρ) and water (bulk modulus K_F, density ρ_F).[a]

Parameter	Value	Unit
E	70	GPa
ν	0.33	
ρ	2700	kg m^{-3}
K_F	2.22	GPa
ρ_F	1000	kg m^{-3}
c_P	6198	ms^{-1}
c_S	3122	ms^{-1}
c_{pR}	2923	ms^{-1}
c_F	1490	ms^{-1}
c_{St}	1487	ms^{-1}
$\lvert I_{pR}\rvert$	1.731×10^6	kg m^{-2} s^{-1}
$\angle I_{pR}$	3.131	
$\lvert I_{St}\rvert$	2.174×10^7	kg m^{-2} s^{-1}
$\angle I_{St}$	$-\pi/2$	
$\lvert E_{pR}\rvert$	0.6404	
$\angle E_{pR}$	-1.458	
$\lvert E_{St}\rvert$	0.2994	
$\angle E_{St}$	$-\pi/2$	

[a]Further, the values of propagation velocities for body wavemodes $c_\alpha = 1/s_\alpha$, $\alpha = \{P, F, S\}$, interface wavemodes $c_\beta = 1/\mathrm{Re}(s_\beta)$, $\beta = \{pR, St\}$, and impedances I_β and ellipticities E_β of the interface wavemodes [Eqs. (16) and (17)] are included.

attributes are less sensitive to the material density ρ of the solid and hence these dependencies are not illustrated here.

III. MEDIUM CHARACTERIZATION

From Fig. 2 it can be observed that for each of the *pR* and *St* waves, the impedance I_β and ellipticity E_β have quite different behaviors in the (E,ν) domain. Obviously, both wave attributes carry the information that is present in the corresponding waveforms of the specific interface wave in a different way. This is an important observation that can be utilized when the impedance and ellipticity are simultaneously exploited to estimate the solid parameters E and ν. In this section we show a way to accomplish this.

We assume that the impedance and ellipticity of a single interface wavemode (*pR* or *St*) can be extracted from multicomponent measurements (u_1, u_3 and p_F; see Sec. V). Then, taking advantage of the different behaviors in the (E,ν) domain, we combine both quantities in a cost function according to[27,28]

$$C_\beta^{I,E}(E,\nu) = \frac{|I_\beta(E,\nu) - I_{\beta,d}|}{2|I_{\beta,d}|} + \frac{|E_\beta(E,\nu) - E_{\beta,d}|}{2|E_{\beta,d}|}. \quad (19)$$

Here, $I_\beta(E,\nu)$ and $E_\beta(E,\nu)$ are model predictions of the impedance and ellipticity (see Fig. 2), and $I_{\beta,d}$ and $E_{\beta,d}$ are the corresponding experimentally observed values (subscript d denotes "data"). The cost function is to be minimized to obtain estimates for E and ν. The two terms on the right-hand side of Eq. (19) are the cost functions related to the impedance and ellipticity separately (C_β^I and C_β^E), respectively (scaled by a factor of 2).

In order to illustrate the behaviors of the cost functions in the (E,ν) domain, we have performed a synthetic test for the water/aluminum configuration; see Table I. Also in Table I, the theoretical values of the impedances and ellipticities computed using Eqs. (16) and (17) are given. Taking these values as representative of the experimental observation $I_{\beta,d}$ and $E_{\beta,d}$, respectively, for both wavemodes we have computed the cost function [Eq. (19)] for varying values of E and ν. As the extraction of the phase of the impedance from combined u_3,p_F measurements can be difficult (see Sec. V), we have only used the magnitudes of the impedances and ellipticities in the cost functions.

For each of the wavemodes the result is illustrated in Fig. 3, where the separate cost functions and the joint cost function are shown. As the separate cost functions do not provide a unique minimum, it is clear that many combinations of E and ν can explain the observed impedance and ellipticity when estimated individually. However, each of the joint cost functions clearly shows a unique minimum, precisely at the values of E and ν of the aluminum (Table I). Unique estimates of E and ν can thus be obtained when the impedance and ellipticity of one of the wavemodes are estimated together. The strength of this approach is that, by combining the wave attributes in the cost function, we simultaneously exploit the information content of the waveforms of an interface wave as present in both the impedance and ellipticity.

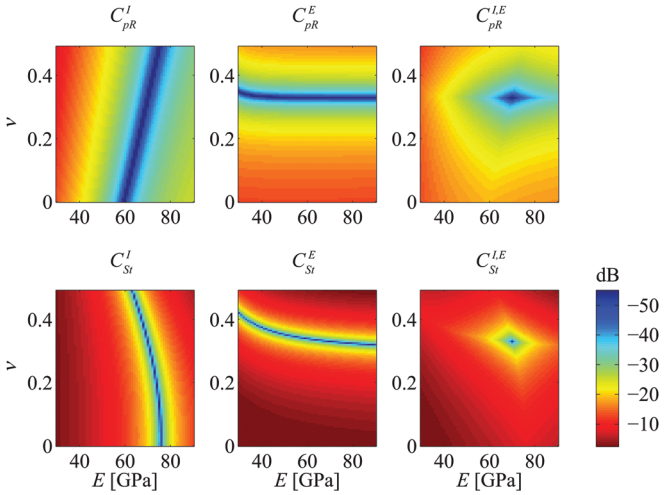

FIG. 3. Separate cost functions for impedances I_β and ellipticities E_β $[\beta = \{pR, St\}]$, and the joint cost functions in which these attributes are combined for each of the wavemodes.

In this numerical test, we have assumed that the values of the impedances and ellipticities can be extracted from the measurements with 100% accuracy. However, in reality this is never the case and therefore it is important to quantify the effect of measurement uncertainties on the estimated values of E and ν. We have perturbed the theoretical values of the impedances ($I_{\beta,d}$) and ellipticities ($E_{\beta,d}$) by $\pm 5\%$ (as an example) and taken the thus obtained values as representative of the experimental observations $I_{\beta,d}$ and $E_{\beta,d}$. Subsequently, we have computed the separate and joint cost functions for four different combinations of $\{I_{\beta,d}, E_{\beta,d}\}$: (1) $\{1.05I_\beta, 1.05E_\beta\}$, (2) $\{0.95I_\beta, 1.05E_\beta\}$, (3) $\{1.05I_\beta, 0.95E_\beta\}$, (4) $\{0.95I_\beta, 0.95E_\beta\}$. For these four cases the estimated values of E and ν (obtained from the locations of the minima of the cost functions) are displayed in Fig. 4 for both the *pR*

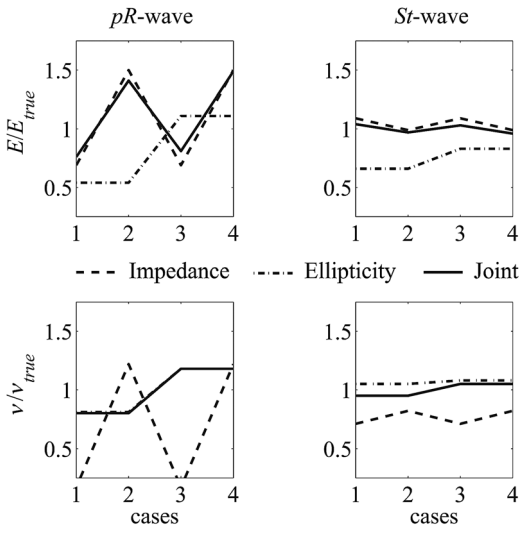

FIG. 4. Estimated values of E and ν for four different combinations of perturbations (cases, as described in the text) of the theoretical impedances and ellipticities, which represent the experimental observations. The results obtained using the individual and the joint cost functions are shown, for both the *pR* and *St* waves. The estimated values of E and ν have been scaled by the corresponding true values of aluminum (see Table I). In the lower left-hand panel the solid and dash-dot lines nearly coincide.

and *St* waves, scaled by the corresponding true values of aluminum (see Table I). It can be seen that the joint cost function does a better job than the individual cost functions for all four cases when the *St* wave is used. This emphasizes that it is beneficial to combine impedance and ellipticity in a joint cost function rather than use these wave attributes individually for the estimation of E and ν: next to the unique estimates, it also offers more stable estimates than the individual cost functions. However, for the *pR* wave the joint cost function does not give the best results in all the cases. For instance, when the impedance (individually) gives a bad estimate for E due to its (relatively) weak sensitivity, the joint cost function also suffers from that weak sensitivity (see Fig. 4, upper left-hand panel, case 4). In that case it is better to use the ellipticity alone. Consequently, the combination of the wave attributes in a cost function is not always beneficial, but when the individual sensitivities are strong enough (as for the *St* wave), this proves to be the case.

From Fig. 4 it can be observed that the estimated values of E and ν can deviate quite significantly from the true values for the *pR* wave, i.e., 49% and 20% at most (for the joint cost function). Using the *St* wave, however, much more stable estimates of E and ν are obtained: at most 4% deviation for E and 5% deviation for ν. This difference between the *pR* and *St* waves is due to the much stronger sensitivity of the *St* wave impedance and ellipticity to E and ν compared to those of the *pR* wave (see Fig. 2), which results in a sharper (see Fig. 3) and, clearly, in a more stable minimum in the joint cost function of the *St* wave.

IV. EXPERIMENT-SPECIFIC MODELING

The above-mentioned estimation of E and ν involves the extraction of impedance and ellipticity of the interface wavemodes from multi-component measurements (u_1, u_3 and p_F). Recently, an elegant way to detect the ellipticity using laser ultrasonics has been reported, showing promising results for the Rayleigh wave at the air/aluminum interface.[13] Similar results can be expected for the fluid/elastic-solid interface waves and therefore, in this paper we restrict ourselves to the extraction of impedance from simultaneous u_3, p_F measurements.

In the experiment we have excited the waves at the fluid/elastic-solid interface using a pulsed laser source that is focused onto a narrow strip on the interface [see Fig. 1(b)]. It approximates an infinitely long line source and creates a thermal diffusion field and acoustic wavefronts that can be considered plane near the excitation site.[12,14,15] Depending on the energy density deposited by the laser pulse, the fields are either generated by the thermoelastic expansion or by ablation forces.[12,29]

The displacement measurement has been performed using a laser Doppler vibrometer (LDV), where the LDV beam crosses the (optically transparent) fluid and is focused on the interface. The pressure measurement has been carried out using a needle hydrophone placed very close to the surface under a small angle with the surface, and just next to the focal point of the LDV beam [see Fig. 1(b)]. Details about the sample, instrumentation and acquisition in the experiment are given in Sec. V.

To investigate the feasibility of the extraction of the interface-wave impedances from the combined u_3,p_F measurements, we now first give the expressions for the acoustic response as excited by the laser source using elastic wave theory [Fig. 1(a); the specific source and the various wavemodes are explained in the following]. We also model the effect of the interference of the LDV beam and the acoustic waves present in the fluid [see Fig. 1(a)]. It is well-known that the optical refractive index of the fluid changes due to pressure variations induced by the acoustic waves.[19] Once the LDV beam and the acoustic waves interfere, the laser light is perturbed. The integrated effect of all perturbations along the LDV beam gives an (undesired) additional contribution to the surface displacement measurement.

A. Acoustic response

As we are only interested in the wave motion, we neglect the optical penetration and the thermal diffusion effects induced by the laser source. In this simplified model, laser excitation in the thermoelastic regime can be modeled by a shear traction dipole loading at the surface.[29] Excitation in the ablation regime can be modeled by a normal force.[12] As we are dealing with excitation in the ablation regime, we use a line force $F(x_1,t)=S(t)\delta(x_1)$ [see Eq. (4)] to model the two-dimensional acoustic response [see Fig. 1(a)]. Here, $\delta(\cdots)$ is the Dirac delta function and $S(t)$ is the time signature of the source representing the energy deposition, which we approximate by the four-point optimum Blackman window function. This is a pulse constituted by the sum of four different cosine functions multiplied with a box function,[7] and its shape is very similar to the Gaussian function that is often employed.[12]

The two-dimensional acoustic response, which is the solution of Eqs. (1)–(5), can be derived using the Cagniard–de Hoop method.[7,30] The result is given in Appendix A. The exact Green's functions are known analytically in the space-time domain and the physical response in u_3 and p_F is found according to [see Eq. (A1)]

$$u_3(\mathbf{x},t) = G_{u_3}(\mathbf{x},t) * S(t), \tag{20}$$

$$p_F(\mathbf{x},t) = G_{p_F}(\mathbf{x},t) * \partial_t S(t), \tag{21}$$

when $0<t<\infty$. Here, the asterisk denotes convolution over time, G_{u_3} and G_{p_F} are the Green's functions of the vertical particle displacement in the solid and of the fluid pressure, respectively [Eqs. (A2) and (A3), and (A11)].

The response is schematically illustrated in Fig. 1(a). It consists of body waves, interface waves, and lateral waves. The body waves are indicated by the solid lines: the compressional (*P*), shear (*S*), and fluid compressional (*F*) waves. The interface waves are indicated by short wavelets: the pseudo-Rayleigh (*pR*) wave and the Stoneley (*St*) wave. Lateral waves, i.e., either head waves (*SP*, *FP*, and *FS*), or the *FpR* wavefront radiated by the *pR* wave, are indicated by dotted lines and addressed by double-mode symbols [see caption to Fig. 1(a)].

B. Effect of optical refractive-index changes integrated along laser beam

Now, we derive a theoretical prediction of the effect of pressure-induced refractive-index changes in the fluid on the LDV measurement. We show how the additional contribution in the measurement is related to the acoustic pressure in the fluid for arbitrary orientation γ of the LDV beam [see Fig. 1(a)].

The location of the LDV beam is determined by the local coordinate ζ along the center of the beam [see Fig. 1(a)]. We denote the (unperturbed) refractive index of the fluid as $n_{F,0}$. Using the photoelastic effect, we can relate a local change (along the LDV beam) in refractive index Δn_F to a change in local pressure p_F as[12]

$$\Delta n_F(\zeta,t) = \frac{\partial n_F}{\partial p_F} p_F(\zeta,t). \tag{22}$$

Now, the locally perturbed wavenumber of the laser light can be written as

$$k_F(\zeta,t) = k_{F,0}\left(1 + \frac{1}{n_{F,0}}\frac{\partial n_F}{\partial p_F} p_F(\zeta,t)\right). \tag{23}$$

Here, $k_{F,0} = n_{F,0}\Omega/v$ is the unperturbed wavenumber, where Ω denotes the angular frequency of the light and v the light wave speed in vacuum. The resulting phase acquired by the optical signal is[18]

$$\theta = \Omega t - 2\int_0^{L(t)} k_F(\zeta,t)d\zeta \tag{24}$$

$$= \Omega t - 2k_{F,0}\big(L_0 + u_{s,\gamma}(t) + u_{f,\gamma}(t)\big), \tag{25}$$

where

$$u_{f,\gamma}(t) = \frac{1}{n_{F,0}}\frac{\partial n_F}{\partial p_F}\int_0^{L(t)} p_F(\zeta,t)d\zeta, \tag{26}$$

and the length of the LDV beam is given as $L(t) = L_0 + u_{s,\gamma}(t)$. Here L_0 is the unperturbed length in the fluid and $u_{s,\gamma}(t)$ is the length variation due to the surface displacement (subscript s) at the focal point; $u_{f,\gamma}(t)$ is discussed in the following. In Eq. (25) it is taken into account that the beam picks up all changes twice.

In the unperturbed situation, the acquired (reference) phase of the optical signal is

$$\theta_{\text{ref}} = \Omega t - 2k_{F,0}L_0. \tag{27}$$

Subtraction of the phase related to the perturbed situation and the reference phase now yields

$$\theta - \theta_{\text{ref}} = -2k_{F,0}\big(u_{s,\gamma}(t) + u_{f,\gamma}(t)\big). \tag{28}$$

From this equation the total LDV-detected signal,

$$u_\gamma(t) = u_{s,\gamma}(t) + u_{f,\gamma}(t), \tag{29}$$

can be readily computed. It consists of two parts: the surface displacement $u_{s,\gamma}(t)$ in the direction γ, which is the desired contribution, and the integral over the refractive-index changes along the LDV beam $u_{f,\gamma}(t)$ [Eq. (26)], which can be interpreted as the additional (virtual) displacement that is measured by the LDV in the fluid (the subscript f refers to the fluid). We address u_γ as the "apparent LDV-detected displacement."

For the line-force excitation at the interface, which is representative of the laser excitation (see Sec. IV A), the acoustic pressure field in the fluid is known [Eq. (21)]. By substitution of this into Eq. (26) we obtain the following expression for the additional displacement:

$$u_{f,\gamma}(t) = \frac{1}{n_{F,0}}\frac{\partial n_F}{\partial p_F}\left(\int_0^{L_0} G_{p_F}(\zeta,t)d\zeta\right) * \partial_t S(t). \tag{30}$$

Due to the use of the Cagniard–de Hoop scheme for the acoustic response, the integrand is known analytically [see Eqs. (A11)–(A15)]. Hence, the integral can be readily evaluated. We note that the upper bound is taken as L_0 because the (linear) pressure field p_F is only defined for the unperturbed geometry of the system. We use Eq. (30) later to quantify the additional contribution to the apparent displacement waveforms, the effect on the extracted impedance (Sec. VI) and the angle dependence of the additional contribution (Sec. VII).

V. EXPERIMENTAL RESULTS AND IMPEDANCE EXTRACTION

In Sec. IV we have briefly introduced the experimental setup that we have used to perform the simultaneous u_3,p_F measurements [see also Fig. 1(b)]. Here, we give the details about the sample, instrumentation, and acquisition, and we show the results that we have obtained accordingly.

The specific configuration that we have used is aluminum in water (see Table I for properties). The aluminum sample with a thickness of 50 mm has been put into an optically transparent water tank made of glass. The water layer thickness is also 50 mm. The excitation laser pulses (produced with a repetition rate of 10 Hz), generated with a broadband Nd:YAG laser, have a duration of 8 ns. A cylindrical lens has been used to focus the beam to a strip of approximately 20 μm wide and 15 mm long.

The LDV (PolyTec®) that we have used for the displacement measurement contains a high-frequency displacement decoder DD-300 having 50 kHz–20 MHz bandwidth. The smoothness and reflectivity of the aluminum sample are sufficiently high to ensure good quality of the LDV signal. The pressure measurement has been carried out using a needle hydrophone HNP-0400 with a preamplifier AH-2010 (Onda®), calibrated over 250 kHz–20 MHz.

During the experiment we have moved the excitation beam over a distance of 29.4 mm in the x_1 direction with steps of $\Delta x_1 = 200$ μm using a scanning stage, keeping the position of the receivers fixed. The smallest source–receiver distance x_0 is 13 mm. For every location of the source, we

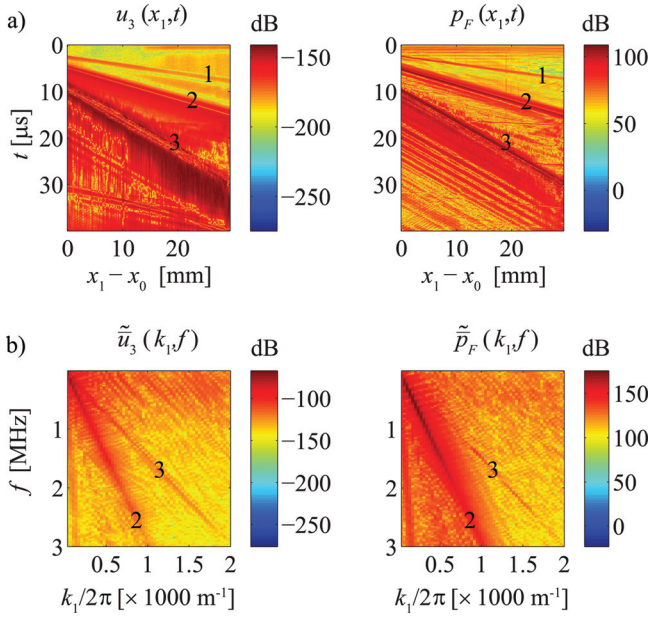

FIG. 5. (a) Observed spatiotemporal evolution of normal particle displacement u_3 (dB re. 1 m) and fluid pressure p_F (dB re. 1 Pa) using a laser Doppler vibrometer and a needle hydrophone, respectively, for a scanning source over a distance of 29.4 mm (the smallest source-receiver distance $x_0 = 13$ mm). The P wave is indicated by (1), the pR wave by (2) and the interfering F- and St-wave arrivals by (3). (b) Corresponding wavenumber-frequency domain spectra $|\tilde{\tilde{u}}_3(k_1,f)|$ and $|\tilde{\tilde{p}}_F(k_1,f)|$, after taping of (x_1,t) data (as described in text). The joint F- and St-wave spectra have not been fully eliminated by the tapering. The P-wave spectra are too weak to be distinguished, but the pR-wave spectra can be clearly identified.

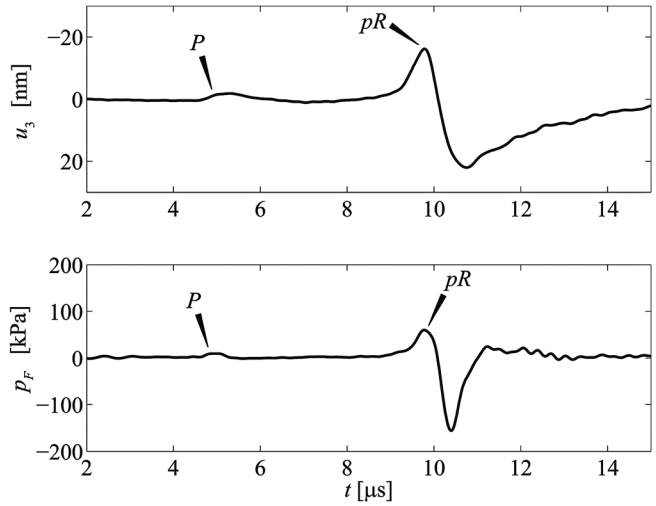

FIG. 6. Observed normal particle displacement u_3 and fluid pressure p_F using a laser Doppler vibrometer and a needle hydrophone, respectively, for source-receiver distance of 28 mm. Only the time window of the P and pR waves is shown. The data have been filtered using a low-pass filter at $f = 3.5$ MHz.

have averaged the signals 256 times to improve the signal/noise ratio.

In Fig. 5(a) the experimentally observed u_3 and p_F are shown. We have applied a low-pass filter at 3.5 MHz to all data to eliminate high-frequency noise. The p_F data have been deconvolved by the frequency-dependent sensitivity of the needle hydrophone/amplifier combination. The u_3 data have been divided by the refractive index of water, $n_{F,0} = 1.333$,[12] because the LDV is calibrated for measurements in air. In Fig. 5(a) we clearly observe the P-wave arrival (~6160 ms^{-1}), the pR-wave arrival (~2960 ms^{-1}) and an interference of the F- and St-wave arrivals (~1500 ms^{-1}); the latter arrivals cannot be distinguished from each other due to the small difference in propagation velocities (see Table I). The observed propagation velocities closely match the predicted values (see Table I). In addition, some (undesired) reflections from the sides and from the sample's back can be distinguished (weak curved arrivals).

In Fig. 6 we show the typical waveforms of the P and pR waves in u_3 and p_F (in this case $x_1 = 28$ mm). We only show the response around these waves because the St wave cannot be distinguished from the less interesting F wave; therefore, we only focus on the extraction of the pR wave impedance.

We have computed the (k_1,f)-domain spectra of u_3 and p_F using a standard two-dimensional Fourier transform algorithm [cf. Eq. (6), where $\omega = 2\pi f$]. Before applying the transforms, the (x_1,t) data have been tapered in time to eliminate a side reflection of the pR wave, which propagates in the same direction as the pR wave of primary interest [see the p_F data of Fig. 5(a), between arrivals 2 and 3]. As a taper function we have used one half-period of a cosine squared covering 2 μs, applied just after the (primary) pR wave and with the same (x_1,t) slope as the F wave. It thus also eliminates the interfering F and St waves, and all subsequent arrivals. In addition, we have tapered the (x_1,t) data near the spatial edges (half-period of cosine squared over 30 samples) and near $t = 0$ (half-period of cosine squared over 0.5 μs) to avoid side effects. The resulting spectra $\tilde{\tilde{u}}_3(k_1,f)$ and $\tilde{\tilde{p}}_F(k_1,f)$ are shown in Fig. 5(b). The combined F,St spectra have not completely been filtered, and the P wave is too weak to be identified. The pR spectra can be clearly distinguished and it is confirmed that the wave propagates without dispersion. The frequency content of the pR wave in $\tilde{\tilde{u}}_3$ is more narrow than that in $\tilde{\tilde{p}}_F$. This is reasonable as the fluid pressure is proportional to the divergence of the displacement, which involves multiplication by ω in the (k_1,ω,x_3) domain; the more narrow frequency content in u_3 can also be observed from the waveforms in Fig. 6.

Now, the impedance $I(k_1,f)$ can be computed from the measured response by division of the two spectra and by $i\omega$. Its magnitude is shown in Fig. 7. This figure shows the advantage of using a scan of measurements as the pR-wave impedance can be easily identified in the (k_1,f) domain. In principle, however, a single source–receiver combination would suffice to extract the impedance in the $(\mathbf{x},f)$ domain. The impedance $|I(k_1,f)|$ is relatively constant over all (k_1,f) combinations that belong to the pR wave, particularly between 0.5 and 1.5 MHz. However, it can be verified that it deviates from the magnitude of the theoretical plane wave impedance [see Eq. (16) and Table I]. The reason is that, apart from measurement inaccuracies, in the displacement measurement also the effect of refractive-index changes along the LDV beam is included, resulting in a modified measurement [see Eq. (29)]. In the next section we quantify this effect.

The phase of the pR-wave impedance cannot be successfully retrieved from $\angle I(k_1,f)$ due to the small but unknown

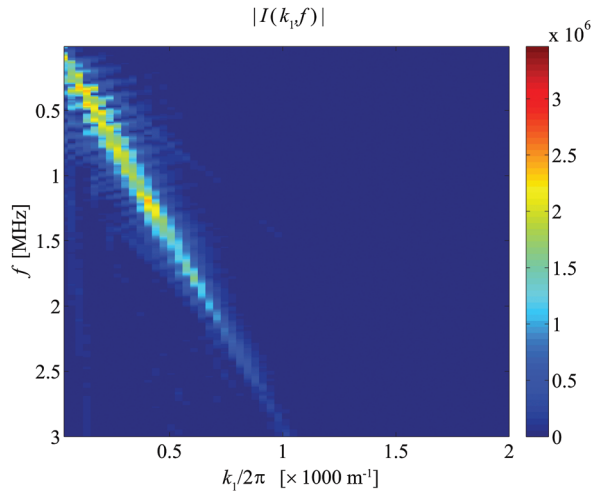

FIG. 7. Magnitude of extracted impedance $I(k_1,f)$ as obtained by division of (the experimentally observed) $\tilde{\tilde{p}}_F(k_1,f)$ and $\tilde{\tilde{u}}_3(k_1,f)$ [see Fig. 5(b)], and by $i\omega$.

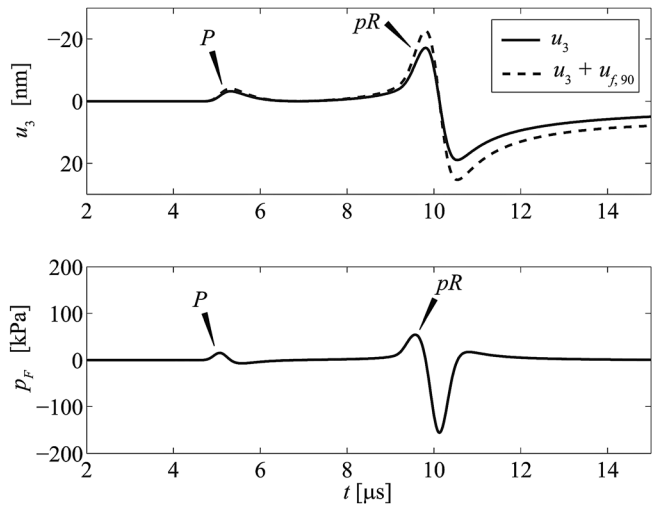

FIG. 8. Modeled normal particle displacement u_3 and fluid pressure p_F for source–receiver distance of 28 mm excited by a line force with $S_{max} = 2.176 \times 10^{-3}$ Nm^{-1} and center frequency $f_0 = 1$ MHz. A prediction of the apparent LDV-detected displacement for $\gamma = 90°$, which includes the effect of refractive-index changes in the trespassed fluid, is also shown [see Eq. (29): u_3 is equivalent to $u_{s,90}$].

difference between the locations of the two detection spots, i.e., the focal point of the LDV beam and the tip of the needle hydrophone [it can be verified that the waveforms in p_F in Figs. 5(a) and 6 arrive slightly later than in u_3]. This results in an additional unknown phase difference.

In conclusion, we can say that the extraction of the *pR*-wave impedance from the simultaneous u_3,p_F measurements at the fluid/elastic-solid interface is feasible. Obviously, the extraction of the *St*-wave impedance is also feasible when this wave can be detected as a separate arrival, i.e., for configurations where its velocity is sufficiently different from the *F*-wave velocity or far away from the generation region, where the *F* wave has vanished in the interface response.

VI. EXPERIMENTAL OBSERVATIONS VERSUS MODEL PREDICTIONS

In this section we compare the experimentally observed waveforms using the laser Doppler vibrometer and the needle hydrophone with modeled equivalents. We quantify the effect of the pressure-induced refractive-index changes integrated along the LDV beam on the predicted waveforms, and evaluate the influence on the impedance extracted from the u_3,p_F measurements.

In Fig. 6 we have shown the typical *P* and *pR* waveforms observed in u_3 and p_F. Now, the corresponding modeled waveforms obtained using the acoustic response at the interface only [Eqs. (20) and (21)] are shown in Fig. 8 (the additional contribution of $u_{f,90}$ is referred to in the following). For the involved fitting parameters we have chosen $S_{max} = 2.176 \times 10^{-3}$ Nm^{-1} (force magnitude) and $f_0 = 1$ MHz (center frequency of the Blackman pulse; Sec. IV A), where we have taken the *pR* waveform in p_F as reference (cf. Figs. 6 and 8). For these choices, the experimentally observed waveforms are very similar to those predicted theoretically. The measured *P* wave in p_F is a bit weaker compared to the predicted result, and in u_3 the observed *pR*-wave magnitude is slightly larger, especially in the tail of the waveform. However, generally the magnitudes are consistent in the two components u_3 and p_F simultaneously, as well as the magnitudes of the *P* and *pR* waves relative to each other in the separate components. In both cases, this is independent of the fitting parameter values. The ripples that are present around 2 μs and immediately after the *pR* wave in Fig. 6 have no modeled equivalents. We consider them as noise. Further, by isolating different contributions in the acoustic response [Eqs. (20) and (21)],[23] it can be shown that there is a weakly excited *S* wave present at the onset of the (modeled) *pR* waveforms.

It can be verified that the smallest wavelength present in the observed responses [Figs. 5(a)–6] is much larger than the width of the focal strip of the excitation laser beam. This validates the line source assumption in the model for the acoustic response, which we have used to compute the theoretical waveforms.

Now, we address the effect of pressure-induced refractive-index changes on the apparent LDV-detected displacement [Eq. (29)]. We have evaluated the integral over ζ in Eq. (30) numerically using an adaptive eight-point Legendre–Gauss algorithm that is able to handle the integrable singularities present in the integrand (i.e., branch points; see Appendix A).[31,32] Using $\partial n_F/\partial p_F = 1.444 \times 10^{-10}$ Pa^{-1} for water at 25°C,[12] a prediction of the additional contribution $u_{f,90}$ can be computed. The result is depicted in Fig. 8 (for $\gamma = 90°$): the (modeled) additional contributions to the waveforms are in phase with and add up to the waveforms in the surface displacement so that the modeled total waveforms are (still) very similar to those observed experimentally (Fig. 6). The influence of $u_{f,90}$ is significant, particularly for the *pR* wave.

To quantify the implication of the modified displacement signal on the extracted *pR*-wave impedance, we have calculated the responses for a scanning source to mimic the experiment using Eqs. (20), (21), and (29), by choosing the same force magnitude and center frequency as discussed previously. A prediction of the magnitude of the modified

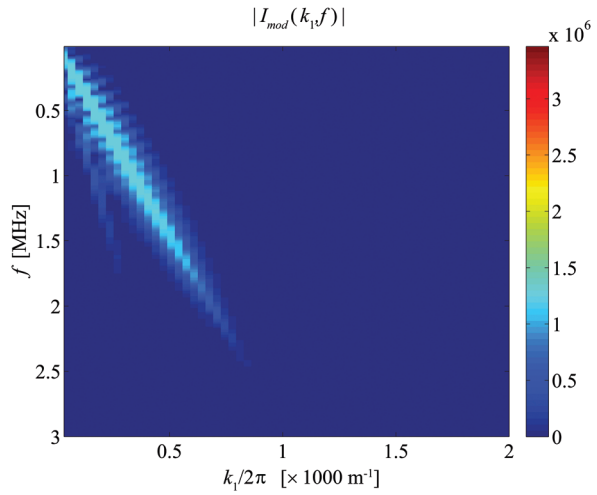

FIG. 9. Predicted magnitude of modified impedance $I_{mod}(k_1, f)$ as obtained by division of the modeled $\tilde{\tilde{p}}_F(k_1,f)$ [Eq. (21)] and $\tilde{\tilde{u}}_{90}(k_1,f)$ [Eq. (29): including the effect of refractive-index changes], and by iω.

impedance $I_{mod}(k_1, f) = \tilde{\tilde{p}}_F/(\mathrm{i}\omega\tilde{\tilde{u}}_{90})$ is shown in Fig. 9 (the same tapering has been applied as for experimental data). To extract the involved modified *pR*-wave impedance $|I_{pR,mod}|$ from $|I_{mod}(k_1,f)|$, we can take the average over all (k_1,f) combinations pertaining to the *pR* wave as the wave is non-dispersive. Incorporating the frequencies 0.5–1.5 MHz, the result is $|I_{pR,mod}| = 0.72|I_{pR}|$. Obviously, the extracted result is smaller than the (theoretical) plane-wave impedance of the *pR* wave. This is consistent with the observation in Fig. 8, where the (prediction of the) apparent LDV-detected displacement is larger than the surface displacement, resulting in larger spectral values in the denominator of $I_{mod}(k_1,f)$.

Comparing the (modeled) modified impedance (Fig. 9) with the impedance as obtained from the measurements (Fig. 7), and taking their averaged values over the mentioned frequency range, we find that the *pR*-wave impedance extracted from the measured data $|I_{pR,d}| = 1.48|I_{pR,mod}|$ [where the subscript *d* refers to the data; cf. Eq. (19)]. This difference between the experiment and the model is quite significant and is, naturally, related to the larger *pR*-wave magnitude in the predicted apparent LDV-detected displacement compared to that in the experimentally observed displacement (cf. Figs. 8 and 6). Based on the measurement inaccuracies in the equipment, the estimated uncertainty in the measurement is roughly $\pm 35\%$, which is smaller than the actual difference. The larger deviation can have several reasons. We believe that it can be due to some calibration error, particularly because the experimentally observed waveforms are almost identical to the modeled equivalents. Another possible cause is a misalignment of the two detection spots (focal point of LDV and tip of needle hydrophone) so that the two measurements are performed at different points on the wavefront. Once the amplitude is not exactly constant over the wavefront [in the x_2 direction; see Fig. 1(a)], this introduces magnitude inconsistencies. Further, the effect of the applied tapers (see Sec. V) on both $|I_{pR,d}|$ and $|I_{pR,mod}|$, which can be estimated using the modeled *pR* waveforms of the interface response [Eqs. (20) and (21)] and the associated theoretical plane-wave impedance I_{pR}, is 5%–10%.

Three-dimensional effects might also have some influence. Most of the used source–receiver distances [see Fig. 5(a)] are larger than the length of the laser strip (in the x_2 direction). For these measurements, the wave propagation is not exactly two-dimensional, which affects the amplitudes and phases of the waveforms with respect to those of the (infinite) line-force situation. However, these amplitude and phase differences are the same for the waveforms in both components (u_3 and p_F). Hence, when their spectral ratio is taken, the amplitude and phase differences are divided out, and the impedance is the same as for the line-force situation that we have assumed (Secs. II and IV); for a proof of this, we refer to Appendix B. Therefore, we argue that the mismatch between the theoretical and experimentally extracted impedances is not due to three-dimensional effects on the waveforms in the interface response. However, the (modeled) additional contribution ($u_{f,\gamma}$) to the LDV measurement that originates from the refractive-index changes along the laser beam [Eq. (26)] will be sensitive to the deviation from the line-force situation. When three-dimensional effects play a role, the pressure magnitude in the fluid (away from the interface) will be smaller due to larger geometrical spreading for a given pressure magnitude at the interface. This will result in a smaller magnitude of $u_{f,\gamma}$ and thus reduce the mismatch between the theoretical and experimentally extracted impedances.

Concerning the possible three-dimensional effects on the waveforms in the interface response, it can be verified that the experimentally observed and modeled waveforms have good similarity for all source–receiver distances (like in Figs. 6 and 8). This shows that the actual wave propagation approximates two-dimensional wave propagation quite well, because otherwise the waveforms would have had different phases (see Appendix B).

VII. DISCUSSION

The additional contribution to the apparent LDV-detected displacement does not only modify the extracted impedance, but also the ellipticity once this would be extracted from a measurement. Hence, for different orientations of the LDV beam (different values of γ), we show the modeled additional contribution $u_{f,\gamma}$ to the apparent displacement in Fig. 10. The magnitude of $u_{f,\gamma}$ varies a little over

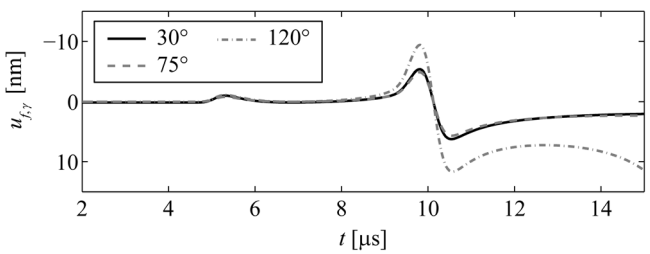

FIG. 10. Prediction of additional contribution to LDV-detected displacements due to pressure-induced refraction-index changes integrated along the laser beam for different orientation angles γ.

$0 < \gamma < 90°$, but the contribution to the *pR* wave rises for $\gamma > 90°$ and becomes slightly broader. This is because γ approaches the angle under which the *FpR* wavefront is radiated by the *pR* wave [149.4°; cf. Fig. 1(a)], which means that the LDV beam and the *FpR* wavefront coincide more and more, and the length over which the beam and the acoustic waves interfere increases. The additional contribution to the *P* wave would also increase once γ approaches the angle of radiation of the *FP*-head wave (166.1°). Obviously, the effect on the ellipticity can be very significant when it is extracted from a measurement where a LDV beam is used with $\gamma > 90°$,[11] or when light scattered in many directions (including $\gamma > 90°$) is collected.[13]

The effect of the involved measurement uncertainties on the estimated values of E and ν using the approach that simultaneously exploits the interface-wave impedance and ellipticity has been evaluated in Sec. III. The adopted perturbations of $\pm 5\%$ for both the experimentally extracted impedances and ellipticities served as an example, but can be realistic once the experimental equipment is recalibrated and/or properly aligned to ensure higher measurement accuracies, and the effect of the refractive-index changes is accounted for.

Further, the parameter-estimation approach (Sec. III) in fact requires three different measurements: u_1, u_3 and p_F. In the proposed method we only estimate two different material parameters (E and ν), for which one of the measurements might seem to be redundant. However, first of all, the combination of the three measurements is beneficial to get unique estimates of the material parameters (see Fig. 3). If, for instance, only the ellipticity would be used, many combinations of E and ν could explain the involved measurements. In addition, we emphasize that impedance and ellipticity are relative quantities, defined as the ratio of two measurements, and as such lack a number of uncertainties that would be present if the absolute measurements were used, e.g., the specific source signature $S(t)$, the specific source distribution in x_1 direction (see Sec. II), and the possible three-dimensional effects (induced by the limited source length in the x_2 direction; see Sec. VI and Appendix B). Hence, effectively we have only two experimentally determined quantities on the basis of which two material parameters can be estimated.

VIII. CONCLUSIONS

The impedance and ellipticity of an interface wave are attributes of the wave that interrelate the full waveforms as observed in the different components. The attributes are defined as the spectral ratios of the fluid pressure at the interface and the normal particle velocity, and of the tangential and normal particle displacements, respectively.

In this paper we showed that, for each of the pseudo-Rayleigh (*pR*) and Stoneley (*St*) waves at the fluid/elastic-solid interface, the impedance and ellipticity have rather different functional dependencies on Young's modulus and Poisson's ratio. By combining the wave attributes in a joint cost function, unique estimates of these parameters can be obtained. Measurement inaccuracies in the impedance and ellipticity can strongly influence the estimated values of Young's modulus and Poisson's ratio when using the *pR* wave. Using the *St* wave, however, very stable estimates are obtained. This illustrates the feasibility of medium characterization using the interface-wave impedance and ellipticity, particularly when exploited simultaneously.

Subsequently, we showed that the impedance of the ultrasonic *pR* wave at the water/aluminum interface can be successfully extracted in the wavenumber-frequency domain. This was accomplished with laser excitation and simultaneous normal particle displacement and fluid pressure measurements using a laser Doppler vibrometer (LDV) and a needle hydrophone, respectively. The *St*-wave impedance could not be extracted in the water/aluminum configuration due to strong interference with the fluid compressional wave.

The extraction of ellipticity has recently been performed by others.[13] The extracted impedance does not only include the fluid pressure and normal particle displacement at the interface (which would give the plane-wave impedance), but also an additional contribution to the displacement measurement due to the interference of the LDV beam, which crosses the fluid, and the acoustic waves in the fluid. The acoustic waves perturb the laser light by modifying the optical refractive index due to pressure variations. By integrating the refractive-index changes along the LDV beam using the modeled fluid pressure field, we predicted that the effect decreases the extracted impedance by some 28% compared to the theoretical plane-wave impedance. The actual impedance extracted from the experiment is, however, 48% larger than this model prediction. As there is excellent agreement between the shape of the observed and predicted *pR* waveforms in both the displacement and fluid pressure, we believe that this difference can be due to a calibration error in the measurement equipment or due to a misalignment in the detection points of the LDV and the needle hydrophone. Three-dimensional effects, which reduce the magnitude of the refractive-index changes, and the applied data processing might also have some influence.

Finally, the great similarity between the observed and predicted *pR* waveforms in both the particle displacement and fluid pressure suggests that, in general, laser ultrasonic sensors and small pressure detectors can be successfully combined in laboratory scale experiments.

ACKNOWLEDGMENTS

For financial support, K.N.v.D. is grateful to The Netherlands Research Centre for Integrated Solid Earth Sciences (ISES), B.S. to the Institute for the Promotion of Innovation through Science and Technology in Flanders, Belgium (IWT-Vlaanderen) (Scholarship No. SB/0661057), and B.V. to SCK-CEN, Belgium and FWO-V, Belgium (Aspirant Scholarship No. C1026). Further, we thank R. Ghose and O. Nishizawa for their constructive ideas, D. J. Rixen and M. Ozbek for their support with the instrumentation, and J. W. Thorbecke for computational assistance.

APPENDIX A: CAGNIARD–DE HOOP SOLUTION

Here, we give the analytical expressions of the Green's functions associated with the vertical particle displacement and fluid pressure in the fluid/elastic-solid configuration excited by a line force applied normal to the interface, i.e., $F(x_1,t)=S(t)\delta(x_1)$ [Eqs. (8) and (9)], where $S(t)$ is the time signature. The functions are obtained using the Cagniard–de Hoop method.[7] We have followed the derivation of Ref. 30 because in there the same transforms are used as we apply [Eq. (6) with $k_1=\omega p_1$]. As the Cagniard–de Hoop method is well-established we only give the outcomes. We assume that $c_S>c_F$ and take x_3 positive downward [see Fig. 1(a)]

The response u_3 in the solid ($x_3\geq 0$) due to the line force is found by convolution of the associated Green's functions $G_{u_3}(\mathbf{x},\tau)$ and the time signature of the force according to

$$u_3(\mathbf{x},t)=\int_0^t S(t-\tau)G_{u_3}(\mathbf{x},\tau)d\tau, \tag{A1}$$

when $0<t<\infty$ and where τ is an auxiliary time variable. The expressions that constitute $G_{u_3}(\mathbf{x},\tau)=G_{u_{3,P}}(\mathbf{x},\tau)+G_{u_{3,S}}(\mathbf{x},\tau)$ read

$$G_{u_{3,P}}=\begin{cases}0, & -\infty<\tau<T_P,\\ \frac{1}{\pi}\mathrm{Im}\left(q_P(\xi_P)\tilde{A}_P(\xi_P)\partial_\tau\xi_P\right), & T_P<\tau<\infty,\end{cases} \tag{A2}$$

$$G_{u_{3,S}}=\begin{cases}0, & -\infty<\tau<T_{SP},\\ \frac{1}{\pi}\mathrm{Im}\left(-\xi_{SP}\tilde{A}_S(\xi_{SP})\right)\partial_\tau\xi_{SP}, & T_{SP}<\tau<T_S,\\ \frac{1}{\pi}\mathrm{Im}\left(-\xi_S\tilde{A}_S(\xi_S)\partial_\tau\xi_S\right), & T_S<\tau<\infty,\end{cases} \tag{A3}$$

where the ξ variables, which replace the p_1 in the arguments, read (with $R^2=x_1^2+x_3^2$),

$$\xi_P=\frac{x_1}{R^2}\tau+\mathrm{i}\frac{x_3}{R^2}\left(\tau^2-T_P^2\right)^{1/2}, \tag{A4}$$

$$\xi_{SP}=\frac{x_1}{R^2}\tau-\frac{x_3}{R^2}\left(T_S^2-\tau^2\right)^{1/2}, \tag{A5}$$

$$\xi_S=\frac{x_1}{R^2}\tau+\mathrm{i}\frac{x_3}{R^2}\left(\tau^2-T_S^2\right)^{1/2}, \tag{A6}$$

$$T_P=Rs_P, \tag{A7}$$

$$T_{SP}=x_1s_S+x_3\left(s_S^2-s_P^2\right)^{1/2}, \tag{A8}$$

$$T_S=Rs_S. \tag{A9}$$

Here, ξ_P denotes the Cagniard path associated with the P wave running into the complex slowness (p_1) plane; ξ_{SP} and ξ_S denote the Cagniard paths associated with the SP-head wave [see Fig. 1(a)] and the S wave, respectively, running along the real p_1 axis and running into the complex p_1 plane. T_P is the arrival time of the P wave, T_{SP} that of SP head wave, and T_S that of the S wave. The SP wave is only present if

$$\frac{x_1}{R}>\frac{s_P}{s_S}. \tag{A10}$$

In Eqs. (A2) and (A3) $\tilde{A}_P$ and $\tilde{A}_S$ are the amplitude factors of the (p_1,x_3,ω)-domain solution in the solid; see Eqs. (7) and (8). The involved square roots (vertical slownesses) $q_\alpha=\left(s_\alpha^2-p_1^2\right)^{1/2}$ are defined such that $\mathrm{Im}(q_\alpha)\leq 0$, $\alpha=\{P, F, S\}$, along the Cagniard paths. The amplitude factors are singular at the body-wave slownesses (branch points) s_α and at the Stoneley pole (s_{St}), which is located at the real p_1 axis and only crossed by the Cagniard paths $\xi_P(\tau>T_P)$ and $\xi_S(\tau>T_S)$ when $x_3=0$ (the St wave arrives later than all other waves).[7] The pseudo-Rayleigh pole lies on another Riemann sheet close to the $\xi_P(x_3=0)$ and $\xi_S(x_3=0)$ paths (see also Sec. II).[9]

The response in the fluid pressure ($x_3\leq 0$) due to the line force is found by convolution of the associated Green's function $G_{p_F}(\mathbf{x},\tau)$ and the time derivative of the force.[7] The expression of $G_{p_F}(\mathbf{x},\tau)$ reads

$$G_{p_F}\begin{cases}0, & -\infty<\tau<T_{FP},\\ \frac{1}{\pi}\mathrm{Im}\left(\tilde{A}_F(\xi_{FP})\right)\partial_\tau\xi_{FP}, & T_{FP}<\tau<T_F,\\ \frac{1}{\pi}\mathrm{Im}\left(\tilde{A}_F(\xi_F)\partial_\tau\xi_F\right), & T_F<\tau<\infty,\end{cases} \tag{A11}$$

where

$$\xi_{FP}=\frac{x_1}{R^2}\tau-\frac{|x_3|}{R^2}\left(T_F^2-\tau^2\right)^{1/2}, \tag{A12}$$

$$\xi_F=\frac{x_1}{R^2}\tau+\mathrm{i}\frac{|x_3|}{R^2}\left(\tau^2-T_F^2\right)^{1/2}, \tag{A13}$$

$$T_{FP}=x_1s_P+|x_3|\left(s_F^2-s_P^2\right)^{1/2}, \tag{A14}$$

$$T_F=Rs_F. \tag{A15}$$

Here, ξ_{FP} and ξ_F denote the Cagniard paths associated with the FP-head wave and the F-body wave, respectively, running along the real p_1 axis and running into the complex p_1 plane. T_{FP} is the arrival time of the FP-head wave [see Fig. 1(a)], and T_F that of the F wave. The FP wave is only present if

$$\frac{x_1}{R}>\frac{s_P}{s_F}. \tag{A16}$$

In Eq. (A11) $\tilde{A}_F$ is the amplitude factor of the (p_1, x_3,ω)-domain solution in the fluid ($x_3\leq 0$); see Eq. (9)

The expressions of the Green's functions are known analytically throughout the entire $(\mathbf{x},t)$ domain; they are used in the main text of the paper.

APPENDIX B: INTERFACE-WAVE IMPEDANCE AND THREE-DIMENSIONAL EFFECTS

In this appendix we show that the interface-wave impedance is not dependent on the specific distribution of the source in the x_2 direction, i.e., that it is not sensitive on

whether the laser strip has finite or infinite length (the latter is assumed in the two-dimensional model in Secs. II and IV).

As an extreme case we first consider the situation of a point force acting on the fluid/solid interface, and compute the far-field interface-wave impedance to show that

$$I_\beta^{(p)}(p_1,x_2,x_3=0,\omega)=I_\beta^{(l)}(p_1,x_3=0,\omega), \tag{B1}$$

where $\beta=\{pR,\ St\}$, the superscripts (p) and (l) refer to "point force" and "line force," respectively, and the expression in the right-hand side denotes the interface-wave impedance as derived in Sec. II [Eq. (16)]. Naturally, we consider the impedances in the same domain, i.e., as the ratio of the Fourier-transformed fluid pressure and normal particle velocity (associated with the interface wave) over time t and horizontal coordinate x_1; the coordinate x_2 thus remains in the argument of the impedance $I_\beta^{(p)}$. For notational convenience, we omit the ω dependence in the arguments of all functions from this point onward.

Starting from three-dimensional equivalents of Eqs. (1) and (2), incorporating a point force $F^{(p)}(x_1,x_2,t)=S(t)\delta(x_1)\delta(x_2)$ in the interface conditions [cf. Eqs. (3)–(5), extended with $\tau_{23}=0$], it can be shown that the far-field interface waves in the (x_1,x_2,x_3,ω) domain at $x_3=0$, when separated from other wavemodes, are described by the corresponding pole residues[23]

$$\hat{u}_{3,\beta}^{(p)}(x_1,x_2,x_3=0)\cong\left(\frac{\omega^3}{2\pi r}\right)^{1/2}\hat{S}\frac{\breve{n}_3^{(p)}(p_r=s_\beta,x_3=0)}{\partial_{p_r}\Delta_{St}|_{p_r=s_\beta}}\times s_\beta^{1/2}e^{-i\omega s_\beta r-i\pi/4}, \tag{B2}$$

$$\hat{p}_{F,\beta}^{(p)}(x_1,x_2,x_3=0)\cong\left(\frac{\omega^3}{2\pi r}\right)^{1/2}\hat{S}\frac{\breve{n}_F^{(p)}(p_r=s_\beta,x_3=0)}{\partial_{p_r}\Delta_{St}|_{p_r=s_\beta}}\times s_\beta^{1/2}e^{-i\omega s_\beta r-i\pi/4}. \tag{B3}$$

Here, $\mathrm{Re}(s_\beta^{1/2})\geq 0$ and $r=(x_1^2+x_2^2)^{1/2}\geq 0$, and the hat represents the (x_1,x_2,x_3,ω) domain. The expressions are accurate in the far field $(|\omega s_\beta r|\gg 1)$. The numerators $\breve{n}_3^{(p)}$ and $\breve{n}_F^{(p)}$ are related to the particle displacement and the fluid pressure in the (p_1,p_2,x_3,ω) domain (p_2 denotes the horizontal slowness associated with x_2), the expressions of which are the starting point to obtain Eqs. (B2) and (B3) using the contour integration method.[23] The expressions read[8]

$$\breve{u}_3^{(p)}=\frac{\breve{n}_3^{(p)}}{\Delta_{St}}\hat{S}=\frac{s_S^2\hat{S}}{i\omega\Delta_{St}}\frac{q_P}{\rho}((s_S^2-2p_r^2)\exp(-i\omega q_P x_3)+2p_r^2\exp(-i\omega q_S x_3)), \tag{B4}$$

$$\breve{p}_F^{(p)}=\frac{\breve{n}_F^{(p)}}{\Delta_{St}}\hat{S}=\frac{s_S^4\hat{S}}{i\omega\Delta_{St}}\frac{\rho_F}{\rho}\frac{q_P}{q_F}\exp(+i\omega q_F x_3), \tag{B5}$$

where the breve $(\breve{u})$ thus refers to the (p_1,p_2,x_3,ω) domain, $p_r=(p_1^2+p_2^2)^{1/2}\geq 0$ is the magnitude of horizontal slowness and $q_\alpha=(s_\alpha^2-p_r^2)^{1/2}$, defined similar as in the line-force situation. In Eqs. (B2) and (B3) the signs of q_α are taken the same as specified in Sec. II.

Remarkably, the expressions for the point-force response in (p_1,p_2,x_3,ω) domain [Eqs. (B4) and (B5)] are very similar to those of the line force [Eqs. (8), (9), and (11)–(13) in Sec. II, with $\tilde{F}=\hat{S}$ for the $\delta(x_1)$ distribution]. The only difference is that in $\breve{u}_3^{(p)}$ the p_r should be replaced by p_1 to obtain $\tilde{u}_3^{(l)}$; here, recall that the tilde refers to the (p_1,x_3,ω) domain.

Now, we Fourier transform the (x_1,x_2,x_3,ω)-domain interface-wave response Eqs. (B2) and (B3) over x_1 [cf. Eq. (6)] in order to compute the impedance $I_\beta^{(p)}(p_1,x_2,x_3=0)$ [Eq. (B1)]. The result can be written as

$$\tilde{u}_{3,\beta}^{(p)}(\bar{p}_1,x_2,x_3=0)\cong\left(\frac{\omega^3}{2\pi}\right)^{1/2}\hat{S}\frac{\breve{n}_3^{(p)}(p_r=s_\beta,x_3=0)}{\partial_{p_r}\Delta_{St}|_{p_r=s_\beta}}\times s_\beta^{1/2}e^{-i\pi/4}\int_{-\infty}^{\infty}\frac{e^{i\omega(\bar{p}_1x_1-s_\beta r)}}{r^{1/2}}dx_1, \tag{B6}$$

$$\tilde{p}_{F,\beta}^{(p)}(\bar{p}_1,x_2,x_3=0)\cong\left(\frac{\omega^3}{2\pi}\right)^{1/2}\hat{S}\frac{\breve{n}_F^{(p)}(p_r=s_\beta,x_3=0)}{\partial_{p_r}\Delta_{St}|_{p_r=s_\beta}}\times s_\beta^{1/2}e^{-i\pi/4}\int_{-\infty}^{\infty}\frac{e^{i\omega(\bar{p}_1x_1-s_\beta r)}}{r^{1/2}}dx_1. \tag{B7}$$

The corresponding expressions for the line-force response $[F^{(l)}=S(t)\delta(x_1)]$ can be found similarly and read

$$\tilde{u}_{3,\beta}^{(l)}(\bar{p}_1,x_3=0)=\omega\hat{S}\frac{\tilde{n}_3^{(l)}(p_1=s_\beta,x_3=0)}{\partial_{p_1}\Delta_{St}|_{p_1=s_\beta}}\times e^{-i\pi/2}\int_{-\infty}^{\infty}e^{i\omega(\bar{p}_1-s_\beta)x_1}dx_1, \tag{B8}$$

$$\tilde{p}_{F,\beta}^{(l)}(\bar{p}_1,x_3=0)=\omega\hat{S}\frac{\tilde{n}_F^{(l)}(p_1=s_\beta,x_3=0)}{\partial_{p_1}\Delta_{St}|_{p_1=s_\beta}}\times e^{-i\pi/2}\int_{-\infty}^{\infty}e^{i\omega(\bar{p}_1-s_\beta)x_1}dx_1. \tag{B9}$$

The $\bar{p}_1$is used in the forward Fourier transform to discriminate it from the p_1 and p_r that have fixed value s_β (and are related to the inverse Fourier transform). Equations (B8) and (B9) are, in principle, only correct in the far field when the interface waves have been separated from other wavemodes.

From comparison of Eqs. (B6) and (B8), and (B7) and (B9), it can now be seen that $\tilde{u}_{3,\beta}^{(p)}(\bar{p}_1,x_2,x_3=0)\neq\tilde{u}_{3,\beta}^{(l)}(\bar{p}_1,x_3=0)$ and $\tilde{p}_{F,\beta}^{(p)}(\bar{p}_1,x_2,x_3=0)\neq\tilde{p}_{F,\beta}^{(l)}(\bar{p}_1,x_3=0)$. Obviously, there are amplitude and phase differences between the waveforms generated by the point force and the line force. However, once the spectral ratio of the fluid pressure and the normal particle displacement is taken, these differences are divided out as they are the same in both components. The impedance in the point-force situation $(I_\beta^{(p)})$ is thus found to be the same as that in the line-force situation $(I_\beta^{(l)})$:

$$I_\beta^{(p)}(\bar{p}_1, x_2, x_3 = 0) = \frac{\tilde{p}_F^{(p)}(p_1 = s_\beta, x_2, x_3 = 0)}{\mathrm{i}\omega \tilde{u}_3^{(p)}(p_1 = s_\beta, x_2, x_3 = 0)}$$
$$= \frac{\breve{n}_F^{(p)}(p_r = s_\beta, x_3 = 0)}{\mathrm{i}\omega \breve{n}_3^{(p)}(p_r = s_\beta, x_3 = 0)}$$
$$= -\frac{\rho_F}{q_F}\bigg|_{p_r = s_\beta}$$
$$= I_\beta^{(l)}(\bar{p}_1, x_3 = 0). \quad \text{(B10)}$$

Here, we note that $\breve{n}_3^{(p)}(p_r = s_\beta, x_3 = 0) = \tilde{n}_3^{(l)}(p_1 = s_\beta, x_3 = 0)$ and $\breve{n}_F^{(p)}(p_r = s_\beta, x_3 = 0) = \tilde{n}_F^{(l)}(p_1 = s_\beta, x_3 = 0)$ [cf. Eqs. (B4) and (8), and Eqs. (B5) and (9)]. Equation (B10) thus proves that $I_\beta^{(p)} = I_\beta^{(l)} = I_\beta$ [see Eq. (16)]. The interface-wave impedance turns out to be independent of frequency (ω) and slowness ($\bar{p}_1$) (see also Sec. II).

The current analysis shows that the far-field interface-wave impedance (generally addressed in the paper as I_β) is the same for both the line-force and the point-force situations. Now, we argue that it is even independent of the specific distribution of the force in x_2 direction as the corresponding effect on the waveforms will always be divided out when the impedance is computed (when both components u_3 and p_F are considered at the same x_2 value). In particular, for a line source of finite length, the space-dependent parts in Eqs. (B6) and (B7) should be convolved with a sinc-function in x_2, but its effect is the same in both the particle-displacement and the fluid-pressure components.

[1]G. J. Rix, "Near-surface site characterization using surface waves," in *Surface Waves in Geomechanics: Direct and Inverse Modelling for Soils and Rocks*, edited by C. G. Lai and K. Wilmanski (CISM, Udine, 2005), pp. 1–46.
[2]C. Glorieux, K. Van de Rostyne, K. Nelson, W. Gao, W. Lauriks, and J. Thoen, "On the character of acoustic waves at the interface between hard and soft solids and liquids," J. Acoust. Soc. Am. **110**, 1299–1306 (2001).
[3]I. A. Viktorov, *Rayleigh and Lamb Waves: Physical Theory and Applications* (Plenum, New York, 1967),Vol. 6, pp. 13, 47–53.
[4]P. G. Malischewsky and F. Scherbaum, "Love's formula and H/V-ratio (ellipticity) of Rayleigh waves," Wave Motion **40**, 57–67 (2004).
[5]L. M. Munirova and T. B. Yanovskaya, "Spectral ratio of the horizontal and vertical Rayleigh wave components and its application to some problems of seismology," Izv. Phys. Solid Earth, **37**, 709716 (2001).
[6]A. M. G. Ferreira and J. H. Woodhouse, "Observations of long period Rayleigh wave ellipticity," Geophys. J. Int. **169**, 161–169 (2007).
[7]A. T. de Hoop and J. H. M. T. van der Hijden, "Generation of acoustic waves by an impulsive line source in a fluid-solid configuration with a plane boundary," J. Acoust. Soc. Am. **74**, 333–342 (1983).
[8]A. T. de Hoop and J. H. M. T. van der Hijden, "Generation of acoustic waves by an impulsive point source in a fluid-solid configuration with a plane boundary," J. Acoust. Soc. Am. **75**, 1709–1715 (1984).
[9]J. H. M. T. van der Hijden, "Quantitative analysis of the pseudo-Rayleigh phenomenon," J. Acoust. Soc. Am. **75**, 1041–1047 (1984).
[10]A. T. de Hoop, *Handbook of Radiation and Scattering of Waves* (Academic, London, 1995), p. 403.
[11]O. Nishizawa, T. Satoh, and X. Lei, "Detection of shear wave in ultrasonic range by using a laser Doppler vibrometer," Rev. Sci. Instrum. **69**, 2572–2573 (1998).
[12]C. B. Scruby and L. E. Drain, *Laser Ultrasonics: Techniques and Applications* (Adam Hilger, New York, 1990), pp. 37–42,76, 243–247, 268, 300–309.
[13]T. E. Blum, K. van Wijk, B. Pouet, and A. Wartelle, "Multicomponent wavefield characterization with a novel scanning laser interferometer," Rev. Sci. Instrum. **81**, 1–4 (2010).
[14]C. Desmet, V. Gusev, W. Lauriks, C. Glorieux, and J. Thoen, "Laser-induced thermoelastic excitation of Scholte waves," Appl. Phys. Lett. **21**, 2939–2941 (1996).
[15]C. Desmet, V. Gusev, W. Lauriks, C. Glorieux, and J. Thoen, "All-optical excitation and detection of leaky Rayleigh waves," Opt. Lett. **22**, 69–71 (1997).
[16]C. Mattei and L. Adler, "Leaky wave detection at air-solid interfaces by laser interferometry," Ultrasonics **38**, 570–571 (2000).
[17]Q. Han, M. Qian, and H. Wang, "Investigation of liquid/solid interface waves with laser excitation and photoelastic effect detection," J. Appl. Phys. **100**, 093101 (2006).
[18]I. Solodov, D. Döring, and G. Busse, "Air-coupled laser vibrometry: Analysis and applications," Appl. Opt. **48**, C33–C37 (2009).
[19]J. F. Allard, M. Henry, C. Glorieux, W. Lauriks, and S. Petillon, "Laser-induced surface modes at water-elastic and poroelastic interfaces," J. Appl. Phys. **95**, 528–535 (2004).
[20]J. D. Achenbach, *Wave Propagation in Elastic Solids* (North-Holland, Amsterdam, 1973), pp. 168–189.
[21]C. P. A. Wapenaar and A. J. Berkhout, *Elastic Wave Field Extrapolation* (Elsevier, Amsterdam, 1989), pp. 12–13.
[22]S. Feng and D. L. Johnson, "High-frequency acoustic properties of a fluid/porous solid interface. I. New surface mode," J. Acoust. Soc. Am. **74**, 906–914 (1983).
[23]K. N. van Dalen, G. G. Drijkoningen, and D. M. J. Smeulders, "Pseudo interface waves observed at the fluid/porous-medium interface. A comparison of two methods," J. Acoust. Soc. Am. **129**, 2912–2922 (2011).
[24]A. D. Pierce, "Basic linear acoustics," in *Springer Handbook of Acoustics*, edited by T. D. Rossing (Springer, New York, 2007), pp. 60–61.
[25]R. D. Borcherdt, *Viscoelastic Waves in Layered Media* (Cambridge University Press, Cambridge, 2009), pp. 206–245.
[26]S. Stein and M. Wysession, *An Introduction to Seismology, Earthquakes, and Earth Structure* (Blackwell, Oxford, 2003), pp. 87–90.
[27]R. Ghose and E. C. Slob, "Quantitative integration of seismic and GPR reflections to derive unique estimates for water saturation and porosity in subsoil," Geophys. Res. Lett. **33**, L05404 (2006).
[28]K. N. van Dalen, R. Ghose, G. G. Drijkoningen, and D. M. J. Smeulders, "*In-situ* permeability from integrated poroelastic reflection coefficients," Geophys. Res. Lett. **37**, L12303 (2010).
[29]I. Arias and J. D. Achenbach, "Thermoelastic generation of ultrasound by line-focused laser irradiation," Int. J. Solid Struct. **40**, 6917–6935 (2003).
[30]C. H. Chapman and J. A. Orcutt, "The computation of body wave synthetic seismograms in laterally homogeneous media," Rev. Geophys. **23**, 105–163 (1985).
[31]P. J. Davis and P. Rabinowitz, *Methods of Numerical Integration* (Academic, London, 1984), pp. 28–34, 425.
[32]M. Abramowitz and I. A. Stegun, *Handbook of Mathematical Functions* (Dover, New York, 1972), pp. 887–888.